The hit-and-return system enables efficient time-resolved serial synchrotron crystallography

Eike C. Schulz[a$], Pedram Mehrabi[a$], Henrike M. Müller-Werkmeister[a,b$], Friedjof Tellkamp[c], Ajay Jha[a], William Stuart[a], Elke Persch[d], Raoul De Gasparo[d], François Diederich[d], Emil F. Pai[e,f,g,h*], R. J. Dwayne Miller[a,i,j*]

[a]Max-Planck-Institute for Structure and Dynamics of Matter, Department for Atomically Resolved Dynamics, Luruper Chaussee 149, 22761 Hamburg, Germany

[b]University of Potsdam, Institute of Chemistry, Physical Chemistry, Karl-Liebknecht-Str. 24-25 14476 Potsdam-Golm, Germany

[c]Max-Planck-Institute for Structure and Dynamics of Matter, Scientific Support Unit Machine Physics, Luruper Chaussee 149, 22761 Hamburg, Germany

[d]Laboratorium für Organische Chemie, ETH Zürich, Vladimir-Prelog-Weg 3, 8093, Zürich, Switzerland.

[e]Department of Biochemistry, University of Toronto, Toronto, Ontario, Canada

[f]Department of Medical Biophysics, University of Toronto, Toronto, Ontario, Canada,

[g]Department of Molecular Genetics, University of Toronto, Toronto, Ontario, Canada,

[h]The Campbell Family Cancer Research Institute, Ontario, Cancer Institute, Toronto, Ontario, Canada,

[i]University of Toronto, Departments of Chemistry and Physics, 80 St. George Street, Toronto, Ontario, M5S 3H6, Canada

[j]Department of Physics, Centre for Ultrafast Imaging – University of Hamburg, Luruper Chaussee 149, Hamburg, 22761, Germany

[$]These authors contributed equally.

[*]corresponding authors: dwayne.miller@mpsd.mpg.de; emil.pai@utoronto.ca

Supplementary Results

Extension of the mini end station with an IR viewing system

Our original fixed target chip (Generation 1: 9x9 compartments, with 12x12 features = 11,664 total features), as well as its recent re-design (Generation 2: 6x6 compartments with 24x24 features = 20,736 total features), have been described previously[9-11]. Briefly, in the crystallography chip crystals are held in a random orientation in precisely defined, bottomless wells or features. At the front side of the chip the features have an opening of 50x50 µm, which reduces to 8x8 µm at their backside to efficiently trap the protein crystals during loading[9, 10, 12]. To increase the stability of the silicon chip these features are organized in to 6x6 compartments with a silicon thickness of 50 µm, surrounded by silicon bars with a thickness of 500 µm. The experimental setup, (**Supplementary Fig. 2**) is slightly modified with respect to the original design[13]. We have extended the mini-end station with an on-axis infrared (IR) viewing system. The IR light source is mounted as a back-light on the beamline while the camera is facing the backside of the chip. Although alignment of the chip can be achieved with light in the visible spectrum, IR has two advantages: firstly, photosensitive samples can be loaded and aligned with high precision and without photo-damage to the system; secondly, chip alignment is improved due to the existence of regions of the chip that are semi-transparent in the IR spectrum, the 50 µm thick compartments. The thicker silicon bars, however, remain opaque (**Supplementary Fig. 6**). Due to this effect, it is not only possible to accurately observe the bottom openings on the chip, but to also determine the positions of protein crystals on the chip surface.

Optical excitation and indirect shuttering

To enable time-resolved pump-probe SSX, we have also introduced a fs-laser source as pump light to the setup, which can be used to either directly initiate a biochemical reaction or trigger the cleavage of a photocaged substrate as in the experiment described in this paper (**Supplementary Fig. 2**). This excitation source's peak power can be exploited to generate a wide variety of excitation wavelengths for 1-photon resonant excitation or multiphoton excitation for virtually all excitation needs. The pump laser beam is introduced to the setup via a path of UV enhanced aluminium mirrors and focussed onto the sample using a prism mirror mounted close to the X-ray capillary. During this experiment the total

laser-energy transmitted to the sample was 45 nJ, ensuring efficient excitation but preventing artificial effects due to dissipation of excess energy. Subsequent pulses from the synchrotron X-ray beam are delivered to probe the structural changes of the target system. In addition to beam brightness, another general hardware limitation in fast time-resolved SSX is very often the speed of the X-ray shutter. Dependent on the experimental design, fast X-ray shutters operate on the order of a few milliseconds with about 10^{10} openings per life cycle and a low repetition rate (~10 Hz). Since our current data collection speed allows recording of $10^6 – 10^7$ diffraction images within 24 h, using the fast X-ray shutter during the pump-probe experiment is not a sustainable approach. Electronic detector shutters, which determine the exposure time of the detector are clearly fast enough for TR-SSX with cycle times of a few milliseconds (i.e. Pilatus 6M) or even microseconds in the case of the latest generation counting detectors (i.e. Eiger 16M). To circumvent the lack of a fast X-ray shutter and simultaneously reduce exposure time of the crystals we apply an '*indirect shuttering'* approach. To this end, we use the high-speed translation stage system and move the protein crystals out of the beam after a diffraction image is recorded (**Supplementary Fig. 4**). The whole system uses the information of the stage as the master clock: 1) the chip moves to a new crystal position; 2) a pulsed signal is generated at the motion controller as soon as the position is reached; 3) this pulse triggers the 15 ms *exposure* of the detector; 4) after this time a 1.02 ms signal is given to the pulse picker of the fs-laser. Since the fs-laser operates at a frequency of 1 kHz, statistically every 1 ms a pulse is generated. By setting the time interval for the pulse picker just above 1 ms, we ensure that at least one pulse is sent to the sample. While the combination of beam brightness and absolute exposure time determines the shortest possible time delays for SSX experiments the situation is different for long time delays. In contrast to liquid jet injection systems, fixed target SFX/SSX experiments have no theoretical limit for long time delays. However, from a practical point of view, time delays longer than a few hundred ms become impractical if every crystal is to be addressed consecutively. To circumvent this problem and drastically reduce the required beamtime even for long time delays we designed the *HARE approach* for SSX/SFX.

Comparison of sequential and HARE time delays

For comparison a single chip using sequential delays would take ~4.7 h (752 ms delay[§] + 72 ms chip translation = 824 ms / crystal * 20,736 features = 284.8 min) while the cumulative data collection takes only ~1h using the HARE delays (8* (72 ms chip translation + 20 ms exposure period + 2 ms laser excitation) = 752 ms / 8 crystals * 20,736 features = 64.9 min). [§]For sequential delays the exposure period and laser excitation would be included in the delay time. [$]exposure period = 15 ms X-ray exposure plus detector opening time.

Accuracy of the timing

To assess the timing accuracy of our setup we have plotted distribution functions of five different time delays for a whole chip (Supplementary Fig. 7). The plot shows the percentage of diffraction images with their deviation in ms from the median. The time delays shown are HARE 2 = 188 ms, HARE 3 = 282 ms, HARE 12 = 1128 ms, HARE 72 = 6768 ms and HARE 144 = 13536 ms. The plot shows the reproducibility of the time delay. For a time delay of 188 ms and 282 ms the deviation from the median value is on the order of +/- 5ms, corresponding to an error of +/- 3.5 % and 2.6 %, respectively. For long time delays the absolute deviation is larger, but the relative error is small, i.e. for the time delay of 13536 ms the maximum deviation from the median value is - 200 ms/ + 150 ms, corresponding to a relative error of max. -1.7 %. By using more refined algorithms and modified motion control electronics one could achieve higher timing accuracies, but with the drawback of a reduced measurement rate. By contrast to liquid sample injection approaches, there is a trade-off between increasing the velocity (>>30 Hz) of the translation stages to its positional accuracy[13]. Importantly, however, the accuracy of the individual time-points would not be affected.

Radiation Damage

To address the concern of X-ray damage, we recorded two dark structures (i.e. without laser-pulses), after 1 (0.28 MGy) and 2 (0.56 MGy) X-ray pulses, respectively. These structures do not show any detectable differences between each other. They also do not show reduced electron density for the cap-domain loop, further substantiating that the reduced electron density we see for this region in the 752 ms and 2052 ms time-points is clearly associated to its biological function (**Supplementary Fig. 10**). Conversely, the longer the reaction of the enzyme is allowed to progress the more structural changes

can be observed, while the cumulative dose never exceeds 0.56 and 0.74 MGy, respectively. In addition, these structural changes fully parallel those of our previous static studies, where we can observe that the disordering of the cap-domain loop is associated with substrate turnover by FAcD (**Supplementary Fig. 11**)[14, 15].

Supplementary Discussion

To truly understand how proteins function one requires a detailed examination of all operating time scales. TRX is one of the few methods available that provide access to the dynamics of biomolecular reactions in structural terms. Since the advent of XFEL sources this relatively well established technique has regained popularity[16-19]. Serial femtosecond crystallography (SFX) re-established this technique as a large series of single-shot experiments, greatly facilitating data collection and providing access to non-reversible reactions in time-resolved experiments (TR-SFX). The problem has been that to date these studies have been restricted to the use of large crystals and conventional data collection methods limiting the scope of potential experiments due to both limited supply of sufficient quality crystals and X-ray damage considerations[16, 20-22]. Only very few of the TRX studies do not rely on reversible, light induced systems and radiation damage of the sample often proves to be a serious problem. With the advent of X-ray free-electron laser (XFEL) sources TRX has re-gained popularity. At XFELs TRX is performed as a series of single-shot experiments in a pump-probe fashion. To this end, a large variety of sample delivery methods has been developed to serve the need to inject thousands to millions of individual micro-crystals into the X-ray beam[9, 10, 23-31].

Since the first demonstration of serial femtosecond crystallography (SFX) many different protein systems have been studied[32-35]. These involved the carbon-monoxide release from myoglobin, structural changes within photosystem I-ferredoxin, the oxygen evolving complex in photosystem II and the trans-cis conformational transition in photoactive yellow protein (PYP)[36-42]. All these systems have in common that they employed liquid jet injectors, were photo-triggered and the majority of time points were in the picosecond or longer domain. To expand the number of accessible systems and address non-photoinducible enzymes three similar *in-situ* mixing methods were described recently[25, 43-45]. Nevertheless, similar to previous approaches these methods focussed on fast time-points, albeit slower time-points should be accessible[43].

Data collection in serial femtosecond crystallography (SFX) is based on the *diffraction-before-destruction* principle[33, 46]. In SFX the diffraction information can be captured on femtosecond time scales based on the durations of the laser excitation pulse, the X-ray probe pulse, and relative time delay between the pump and probe. This has two advantages: the first is the ultra-short time of the

probe pulses that even enable the capture of intermediates of ultra-fast processes such as bond-vibration, base-wobbling, global twisting and side-chain rotations[47]. The second advantage is the absence of most radiation damage effects, as the diffraction process and thereby data generation stops well before major secondary damage processes commence. In SFX, data collection is thus based on the recording of thousands of still images of individual crystals, where every crystal is exposed to a high-intensity X-ray pulse only once. For studying ultrafast time-resolved structural changes in biological macromolecular systems involving 10 micron scale crystals, XFEL sources are currently the only tools available that provide a temporal resolution on the femtosecond to nanosecond timescale. However, serial crystallography is not limited to XFELS but can also be conducted at synchrotron sources (serial synchrotron crystallography - SSX). The general principle in SSX is largely the same as in SFX, with the advantage of much better availability of SSX beamtime generating increased potential for structural biology applications.

Sample-transfer and reaction initiation systems

In addition to optically triggered systems the "mix-and-inject" approach was introduced for XFELs[44, 45]. Here the crystal suspension and the ligand solution are transferred through a T-junction mixer before ejection into the XFEL beam. One of the current limitations with this approach lies in the population mixing that can result from the laminar flow in the capillary[25]. However, more importantly the liquid jet technology does not allow to address time-points below 30 ms or higher than 2000 ms. Modifications of these time-ranges would require changes to the flow-rate, and major hardware alterations to the device [44]. In comparison to liquid jet injectors the tape-drive technology appears to bear higher potential for time-resolved studies on biologically relevant time-scales. At the moment, two different approaches have been described: Based on XFEL experiments, the "drop-on-tape" approach was described also offering time ranges with higher temporal flexibility than liquid-jet injectors [25]. However, different time-delays require modifications to the laser setup or the transfer speed of the belt [25]. For synchrotron radiation experiments, the "mix-and-diffuse" approach similar to "mix-and-inject" system, was described [43, 45]. However, while the "mix-and-inject system" cannot address time-points longer than 2 s, the "mix-and-diffuse system" was reported to be unable to

measure time points shorter than 2 s or longer than 50 s without significant hardware revision. In addition, the tape-drive system suffers from higher background scattering due to larger path length for the X-rays through large droplets (~280 µm) and polymer scattering from the belt material. With increasing time-delays background scattering from dehydrating droplets as well as PEG interactions with helium could become problematic.

Conversely, in our system most of the solvent is removed when the crystals are fixed to the chip. In contrast to our approach, it currently appears difficult for the above mentioned systems to quickly change between various time delays. By contrast our setup requires no hardware modifications only quick changes in input parameters to sample time-points ranging from a few milliseconds to several minutes if large portions of the chip are sampled. Additionally, our setup provides the advantage of obtaining a dark-reference pattern for every crystal measured, which can potentially be turned into a novel data-analysis method [48]. However, the most substantial advantage of our HARE approach is that it provides a solution for sampling very slow time-points with comparable throughput to that of fast time-points, in contrast especially to the tape drive approach.

Radiation Damage

Unfortunately, there are currently only very few studies addressing radiation damage for room-temperature diffraction measurements and none that would specifically address this question for serial crystallography. Important differences for room temperature data collection are the *rate* of diffusion of free radical through the crystal lattice, the quenching of radicals by solvent molecules and most importantly free-radical recombination, which is ~10^7 times faster at room temperature than under cryo conditions[49]. Here, each crystal was probed with X-rays of the indicated energy (**Supplementary Table 1, 2**). For those time-points that were recorded using the HARE approach (752 ms, 2052 ms) each crystal was exposed twice, hence the total dose was 0.56 MGy and 0.74 MGy, respectively depending on the beamline. The Garman-limit for a cryo-cooled crystal lies at 43 MGy, while for room-temperature crystals the old Blake and Phillips value of 0.59 MGy is often quoted [50, 51]. Our cumulative dose is either below this conservative level or only slightly exceeds this value. However, recently an inverse dose-rate effect was demonstrated for room-temperature data showing a positive

linear relationship between dose-tolerance and dose-rate providing an up to >110-fold increase in dose-tolerance [52, 53]. The dose rate for our data-collection was at $5*10^{12}$ ph/s (10 MGy/s), while the inverse dose-rate effect was even observed at 10^8 ph/s, suggesting a more pronounced effect in our case. Consistent with the initial report, the inverse dose rate effect was later on demonstrated in a different study for a number of additional systems but with beam parameters highly comparable to ours. A clear lag-phase of >0.5 MGy was demonstrated for dose rates of ~1 MGy/s, where no loss of diffraction power can be observed [54]. Although these data were recorded comparably rapidly, the total data collection exceeded hundreds of milliseconds, while our data were collected within a short single 37 ms pulse. In combination with the ~10 times higher dose-rate we assume that the lag-phase for our experiment would exceed the 0.5 MGy value. In addition, the authors addressed the question of sample heating and found no significant increase in temperature, even for dose rates of ~25 MGy/s. In conclusion, previous experiments suggest that the dose-rates and cumulative doses applied in our work do not lead to major radiation damage. This is corroborated by our structural findings demonstrating equivalent electron density distributions for the different radiation doses.

Biological implications

Our previous studies have shown that the loss of order of the cap-domain loop is associated with the biological function of FAcD and is not induced by X-ray damage [14, 15]. We have determined several static, isomorphous structures, where both cap domains are present that support this finding (apo-structures collected on a home source – PDB-ID: 5T4T, on a synchrotron - PDB-ID: 3R41, and an SSX structure ablated by an IR-pulse – PDB-ID: 5NYV, respectively). In structures that were co-crystallized with various ligands the electron density for one or both cap domains is missing (measured on a home source - PDB-ID: 5K3F, 5K3E, 5K3B). In structures soaked with various ligands, one or both cap domains are missing (measured on home source and on a synchrotron beamline – PDB-ID: 3R3X, 3R3W, 3R3Y, 3R3V). Thus the increasing disorder in the cap-domain is indeed a mechanistic feature presenting during the catalytic cycle of FAcD. Consequently, we can observe the structural changes that are taking place during binding of the ligand and the subsequent increase in dynamics of the active site. The 752 ms time-point shows a Michaelis-complex (substrate

bound complex) of a catalytically active enzyme. In contrast, all previously described Michaelis complexes of FAcD were chemically trapped via a catalytically inactive mutant. However, in contrast to previous studies this time-resolved experiment investigates the wild-type enzyme at room temperature and hence reflects true snapshots of a '*molecular movie'* of the catalytic process.

Outlook

With the current limitation of available XFEL beamtime, the ability to conduct TR-SSX experiments at widely accessible synchrotron sources offers a major advantage to the structural biology community. Due to the current limitations in brightness of synchrotron sources, studies of nano-crystals or ultrafast time-scale structural dynamics still need to be conducted at XFELs. However, further increases in synchrotron brightness and improved detector technology promise to push this limit to the microsecond domain. Another possibility to increase the temporal resolution for time-resolved synchrotron crystallography includes a Hadamard Transformation based approach, which would also benefit from the technical setup described here [55]. Concordantly, the latter lays the groundwork to address questions about biological and enzymatic systems that could not be addressed previously. Its simplicity allows for easy transfer to other beamlines and requires little specialized training. Most importantly, currently the HARE approach offers the greatest versatility in addressing the biologically relevant timescales of enzymatic reactions in the millisecond to seconds time-scale.

References

1. Oghbaey, S. et al. Fixed target combined with spectral mapping: approaching 100% hit rates for serial crystallography. *Acta Crystallogr D Struct Biol* **72**, 944-955 (2016).
2. Owen, R.L. et al. Low-dose fixed-target serial synchrotron crystallography. *Acta Crystallographica Section D-Structural Biology* **73**, 373-378 (2017).
3. Schulz, E.C. et al. Protein crystals IR laser ablated from aqueous solution at high speed retain their diffractive properties: applications in high-speed serial crystallography. *Journal of Applied Crystallography* **50**, 1773-1781 (2017).
4. Mueller, C. et al. Fixed target matrix for femtosecond time-resolved and in situ serial micro-crystallography. *Struct Dynam-Us* **2** (2015).
5. Sherrell, D.A. et al. A modular and compact portable mini-endstation for high-precision, high-speed fixed target serial crystallography at FEL and synchrotron sources. *Journal of Synchrotron Radiation* **22**, 1372-1378 (2015).
6. Chan, P.W., Yakunin, A.F., Edwards, E.A. & Pai, E.F. Mapping the reaction coordinates of enzymatic defluorination. *J Am Chem Soc* **133**, 7461-7468 (2011).
7. Kim, T.H. et al. The role of dimer asymmetry and protomer dynamics in enzyme catalysis. *Science* **355** (2017).
8. Moffat, K. Time-resolved crystallography. *Acta Crystallogr A* **54**, 833-841 (1998).
9. Moffat, K. Ultrafast time-resolved crystallography. *Nat Struct Biol* **5 Suppl**, 641-643 (1998).
10. Neutze, R. Opportunities and challenges for time-resolved studies of protein structural dynamics at X-ray free-electron lasers. *Philos Trans R Soc Lond B Biol Sci* **369**, 20130318 (2014).
11. Neutze, R. & Moffat, K. Time-resolved structural studies at synchrotrons and X-ray free electron lasers: opportunities and challenges. *Curr Opin Struct Biol* **22**, 651-659 (2012).
12. Gai, F., Hasson, K.C., McDonald, J.C. & Anfinrud, P.A. Chemical dynamics in proteins: the photoisomerization of retinal in bacteriorhodopsin. *Science* **279**, 1886-1891 (1998).
13. Neutze, R. Opportunities and challenges for time-resolved studies of protein structural dynamics at X-ray free-electron lasers. *Philos T R Soc B* **369** (2014).
14. Westenhoff, S. et al. Time-resolved structural studies of protein reaction dynamics: a smorgasbord of X-ray approaches. *Acta Crystallogr A* **66**, 207-219 (2010).
15. Chavas, L.M., Gumprecht, L. & Chapman, H.N. Possibilities for serial femtosecond crystallography sample delivery at future light sources. *Struct Dyn* **2**, 041709 (2015).
16. DePonte, D.P. et al. Gas dynamic virtual nozzle for generation of microscopic droplet streams. *J Phys D Appl Phys* **41** (2008).
17. Fuller, F.D. et al. Drop-on-demand sample delivery for studying biocatalysts in action at X-ray free-electron lasers. *Nat Methods* **14**, 443-449 (2017).
18. Nelson, G. et al. Three-dimensional-printed gas dynamic virtual nozzles for x-ray laser sample delivery. *Opt Express* **24**, 11515-11530 (2016).
19. Oberthuer, D. et al. Double-flow focused liquid injector for efficient serial femtosecond crystallography. *Sci Rep* **7**, 44628 (2017).
20. Roedig, P. et al. High-speed fixed-target serial virus crystallography. *Nat Methods* (2017).
21. Sierra, R.G. et al. Concentric-flow electrokinetic injector enables serial crystallography of ribosome and photosystem II. *Nat Methods* **13**, 59-62 (2016).
22. Weierstall, U. et al. Lipidic cubic phase injector facilitates membrane protein serial femtosecond crystallography. *Nat Commun* **5**, 3309 (2014).
23. Zarrine-Afsar, A. et al. Crystallography on a chip. *Acta Crystallogr D Biol Crystallogr* **68**, 321-323 (2012).
24. Boutet, S. et al. High-resolution protein structure determination by serial femtosecond crystallography. *Science* **337**, 362-364 (2012).

25. Chapman, H.N. et al. Femtosecond X-ray protein nanocrystallography. *Nature* **470**, 73-77 (2011).
26. Liu, W. et al. Serial femtosecond crystallography of G protein-coupled receptors. *Science* **342**, 1521-1524 (2013).
27. Redecke, L. et al. Natively inhibited Trypanosoma brucei cathepsin B structure determined by using an X-ray laser. *Science* **339**, 227-230 (2013).
28. Aquila, A. et al. Time-resolved protein nanocrystallography using an X-ray free-electron laser. *Optics Express* **20**, 2706-2716 (2012).
29. Arnlund, D. et al. Visualizing a protein quake with time-resolved X-ray scattering at a free-electron laser. *Nat Methods* **11**, 923-926 (2014).
30. Kupitz, C. et al. Serial time-resolved crystallography of photosystem II using a femtosecond X-ray laser. *Nature* **513**, 261-265 (2014).
31. Schotte, F. et al. Watching a signaling protein function in real time via 100-ps time-resolved Laue crystallography. *P Natl Acad Sci USA* **109**, 19256-19261 (2012).
32. Schotte, F. et al. Watching a protein as it functions with 150-ps time-resolved X-ray crystallography. *Science* **300**, 1944-1947 (2003).
33. Suga, M. et al. Light-induced structural changes and the site of O=O bond formation in PSII caught by XFEL. *Nature* **543**, 131-135 (2017).
34. Tenboer, J. et al. Time-resolved serial crystallography captures high-resolution intermediates of photoactive yellow protein. *Science* **346**, 1242-1246 (2014).
35. Beyerlein, K.R. et al. Mix-and-diffuse serial synchrotron crystallography. *IUCrJ* **4**, 769-777 (2017).
36. Stagno, J.R. et al. Structures of riboswitch RNA reaction states by mix-and-inject XFEL serial crystallography. *Nature* **541**, 242-246 (2017).
37. Neutze, R., Wouts, R., van der Spoel, D., Weckert, E. & Hajdu, J. Potential for biomolecular imaging with femtosecond X-ray pulses. *Nature* **406**, 752-757 (2000).
38. Fenwick, R.B., Esteban-Martin, S. & Salvatella, X. Understanding biomolecular motion, recognition, and allostery by use of conformational ensembles. *Eur Biophys J Biophy* **40**, 1339-1355 (2011).
39. Coppens, P. et al. The RATIO method for time-resolved Laue crystallography. *J Synchrotron Radiat* **16**, 226-230 (2009).
40. Garrett, B.C. et al. Role of water in electron-initiated processes and radical chemistry: issues and scientific advances. *Chem Rev* **105**, 355-390 (2005).
41. Owen, R.L., Rudino-Pinera, E. & Garman, E.F. Experimental determination of the radiation dose limit for cryocooled protein crystals. *Proc Natl Acad Sci U S A* **103**, 4912-4917 (2006).
42. Blake, C.C.F. & Phillips, D.C. in Biological Effects of Ionizing Radiation At the Molecular Level (Vienna; 1962).
43. Garman, E.F. Radiation damage in macromolecular crystallography: what is it and why should we care? *Acta Crystallogr D Biol Crystallogr* **66**, 339-351 (2010).
44. Southworth-Davies, R.J., Medina, M.A., Carmichael, I. & Garman, E.F. Observation of decreased radiation damage at higher dose rates in room temperature protein crystallography. *Structure* **15**, 1531-1541 (2007).
45. Owen, R.L. et al. Exploiting fast detectors to enter a new dimension in room-temperature crystallography. *Acta Crystallogr D Biol Crystallogr* **70**, 1248-1256 (2014).
46. Beddard, G.S. & Yorke, B.A. Pump-Probe Spectroscopy Using the Hadamard Transform. *Appl Spectrosc* **70**, 1292-1299 (2016).

Supplementary Tables

Supplementary Table 1. Data collection and refinement statistics.

Accession Code (Delay time)	6GXH (0 ms)	(6FSX) 30 ms	(6GXD) 752 ms	6GXT (2,052 ms)	6GXF (RadDam1)	6GXL (RadDam2)
Data collection						
Space group	$P2_1$	$P2_1$	$P2_1$	$P2_1$	$P2_1$	$P2_1$
Cell dimensions						
a, b, c (Å)	42.1 79.97 84.79	41.78, 79.38, 84.47	41.37, 78.54, 83.51	41.76, 79.54, 84.46	41.30, 78.56, 83.57	41.32, 78.54, 83.56
α, β, γ (°)	90.0, 102.9, 90.0	90.0, 102.9, 90.0	90.0, 102.8, 90.0	90.0, 102.9, 90.0	90.0, 102.9, 90.0	90.0, 102.9, 90.0
Resolution (Å)	86.13 - 1.80 (1.83 - 1.80)	82.46 - 1.80 (1.83 - 1.80)	81.50 - 1.80 (1.83 - 1.80)	57.51 - 1.95 (2.00 - 1.95)	81.42 - 1.80 (1.83 - 1.80)	81.42 - 1.80 (1.83 - 1.80)
$CC_{1/2}$	96.7 (60.0)	98.0 (86.4)	90.1 (67.1)	88.4 (55.7)	74.74 (41.1)	71.0 (39.6)
I/s (I)	8.8 (3.7)	11.1 (5.8)	5.3 (3.3)	4.0 (1.8)	2.9 (2.1)	3.0 (2.1)
Completeness (%)	99.9 (99.9)	100.0 (99.9)	100 (100)	99.9 (99.9)	99.8 (99.4)	99.9 (99.6)
Multiplicity	132.2 (70.4)	268.3 (200.3)	39.5 (25.7)	59.2 (45.7)	9.2 (6.3)	9.5 (6.5)
Refinement						
Resolution range (Å)	57.47-1.80	82.35-1.80	40.72-1.80	57.20-1.95	40.72-1.80	40.72-1.80
No. reflections	50455	49794	48304	39350	48165	48202
R_{work} (%) / R_{free} (%)	18.74 / 23.59	16.78 / 21.07	16.51 / 20.9	18.15 / 22.77	22.19 / 26.9	21.58 / 26.04
No. atoms						
Protein atoms	4722	4786	4815	4756	4748	4748
Ligand/ion	0	2	7	10	0	0
water	261	246	443	186	412	412
B-factors						
protein	25.93	22.94	21.12	27.87	21.14	24.5
Ligand/ion	0	43.55	26.69	26.47	0	0
water	33.06	34.33	34.16	34.91	32.31	32.68
R.m.s. deviations						
Bond length(Å)	0.007	0.012	0.016	0.008	0.006	0.007
Bond angles (°)	0.864	1.293	1.55	0.905	0.82	0.927

Number of crystals (images) for earch structure is shown in Supplementary Table 2 * Values in parenthesis show the data in the outer resolution shell.

Supplementary Table 2. Additional data collection and Ramachandran statistics

Delay time	0 ms	30 ms	752 ms	2,052 ms	RadDam1	RadDam2
Data collection						
Diffraction weighted dose per crystal (MGy)	0.37	0.37	0.56	0.74	0.28	0.56
Exposure time (s)	0.037	0.037	0.015	0.037	0.015	0.015
Energy (keV)	12.7	12.7	12.1	12.7	12.1	12.1
Flux (ph/s)	5.00E+12	5.00E+12	1.00E+13	5.00E+12	1.00E+13	1.00E+13
Beam size (µm)	5 x 9	5 x 9	4 x 9	5 x 9	4 x 9	4 x 9
Wavelength (Å)	0.97626	0.97626	1.0089	0.97626	1.0089	1.0089
Number of images included in scaling	17128	23900	3318	5203	967	1008
Wilson B-factor Å2	24.46	21.02	18.74	27.06	20.1	22.3
Reflections observed	6678211 (576427)	13358810 (1605982)	1910702 (200204)	2330728 (288294)	443142 (48861)	458342 (50579)
Reflections unique	50502 (8192)	49797 (8019)	48357 (7783)	39351 (6312)	48178 (7716)	48210 (7733)
Reflections used for R-free	2561	1630	2388	1863	2387	2389
Ramachandran statistics						
Favoured (%)	97.12	96.77	97.47	97.12	96.13	96.3
Allowed (%)	2.88	2.89	2.36	2.71	3.37	3.03
Outliers (%)	0	0.34	0.17	0.17	0.51	0.67

* Values in parenthesis show the data in the outer resolution shell

Supplementary Notes

Synthesis of the photocaged Fluoroacetate (pHP-FAc)

General Remarks

The melting point (m.p.) was measured on a Büchi M-560 apparatus in open capillaries. ^{1}H NMR, ^{13}C NMR, and ^{19}F NMR spectra were recorded on Bruker AV III 400 and 500 spectrometers at 25 °C; chemical shifts (δ) are reported in ppm using the residual solvent peak as reference. Atom to peak assignment was based on COSY, HSQC, and HMBC experiments. The infrared (IR) spectrum was recorded on a Perkin-Elmer Spectrum Two IR spectrometer, with the relative peaks intensities described as s (strong), m (medium) or w (weak), with br. (broad) if applicable. High-resolution electrospray ionization mass spectroscopy (HR-ESI-MS) was measured on a Bruker maXis spectrometer, and elemental analysis was measured with a LECO CHN/900 instrument.

Reaction Scheme and Procedure

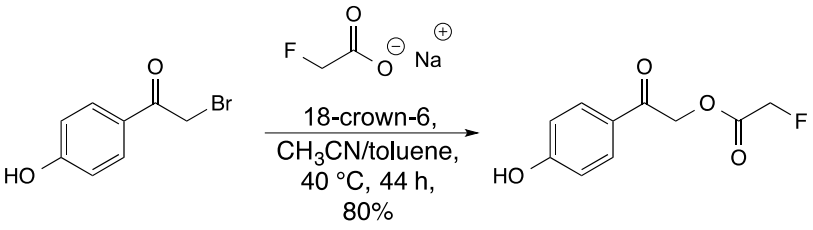

Scheme S1. Reaction for the preparation of photocaged fluoroacetate (pHP-FAc)

2-(4-Hydroxyphenyl)-2-oxoethyl 2-fluoroacetate

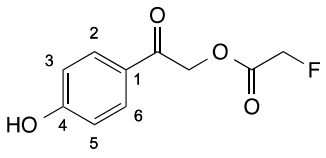

A solution of sodium 2-fluoroacetate (1.02 g, 10.23 mmol) in dry CH_3CN/toluene 1:1 (100 mL) under an Argon atmosphere was treated with 18-crown-6 (2.70 g, 10.23 mmol) and 2-bromo-1-(4-hydroxyphenyl)ethanone (2.00 g, 9.30 mmol), stirred at 40 °C for 44 h, and the solvents were evaporated. Purification by flash chromatography (SiO_2; CH_2Cl_2/MeOH gradient 100:0 to 98:2) gave the product (1.58 g, 80%) as white crystals.

R_f = 0.23 (SiO_2; CH_2Cl_2/MeOH 99:1); m.p. 154–158 °C; ^{1}H NMR (400 MHz, CD_3OD): δ = 5.08 (d, J = 46.8 Hz, 2 H; CH_2F), 5.50 (s, 2 H; CH_2O), 6.85–6.92 (m, 2 H; H–C(3,5)), 7.82–7.93 ppm (m, 2 H; H–C(2,6)); ^{13}C NMR (101 MHz, CD_3OD): δ = 67.48 (d, ^4J(C,F) = 1.2 Hz; CH_2O), 78.62 (d, ^1J(C,F) = 178.6 Hz; CH_2F), 116.58 (C(3,5)), 126.97 (C(1)), 131.54 (C(2,6)), 164.57 (C(4)), 169.39 (d, ^2J(C,F) = 22.4 Hz; CH_2FC=O), 192.07 ppm (OCH_2C=O); ^{19}F NMR (470 MHz, CD_3OD): δ = –233.20 ppm (t, J = 46.7 Hz); IR (ATR): $\tilde{\nu}$ = 3205 (br., s), 2931 (w), 1771 (s), 1660 (m), 1576 (s), 1370 (m), 1206 (s), 1176 (s), 1078 (s), 962 (m), 841 (m), 698 cm^{-1} (m); HR-ESI-MS: m/z (%): 211.0410 (100, $[M - H]^-$, calcd for $C_{10}H_8FO_4^-$: 211.0412); elemental analysis calcd (%) for $C_{10}H_9FO_4$ (212.18): C 56.61, H 4.28, F 8.95; found: C 56.57, H 4.33, F 8.90.

NMR spectra

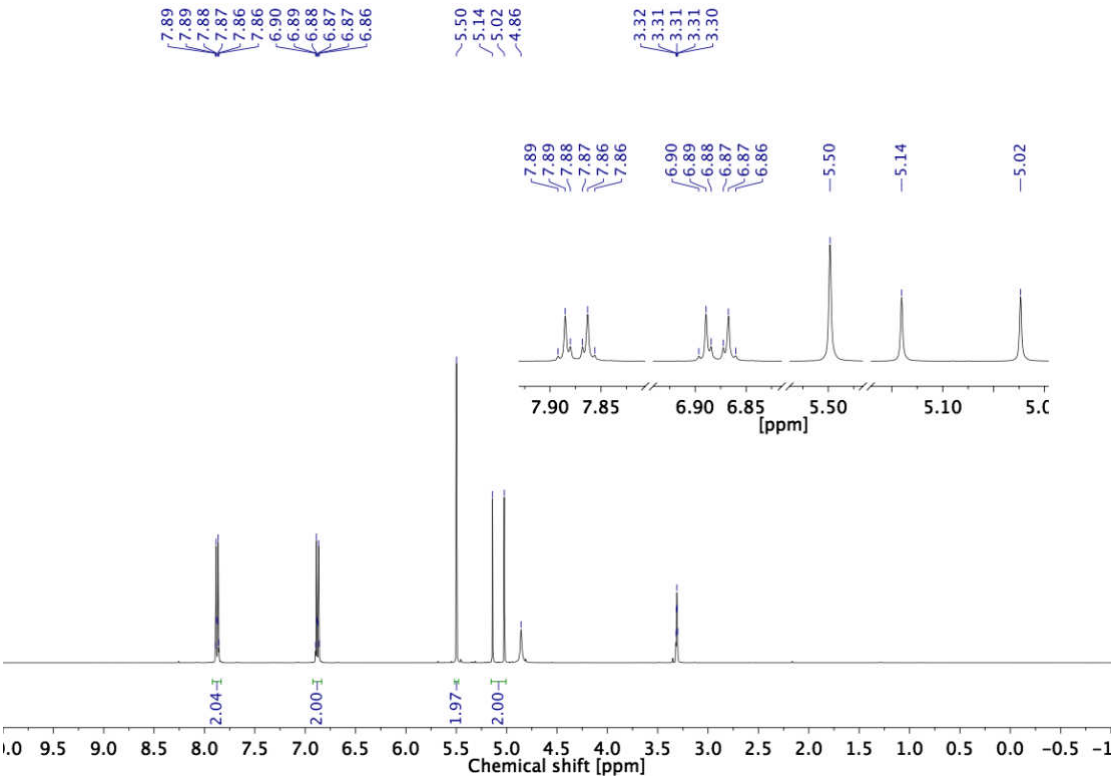

Figure SN1: ^{1}H NMR (400 MHz, 298 K, CD_3OD).

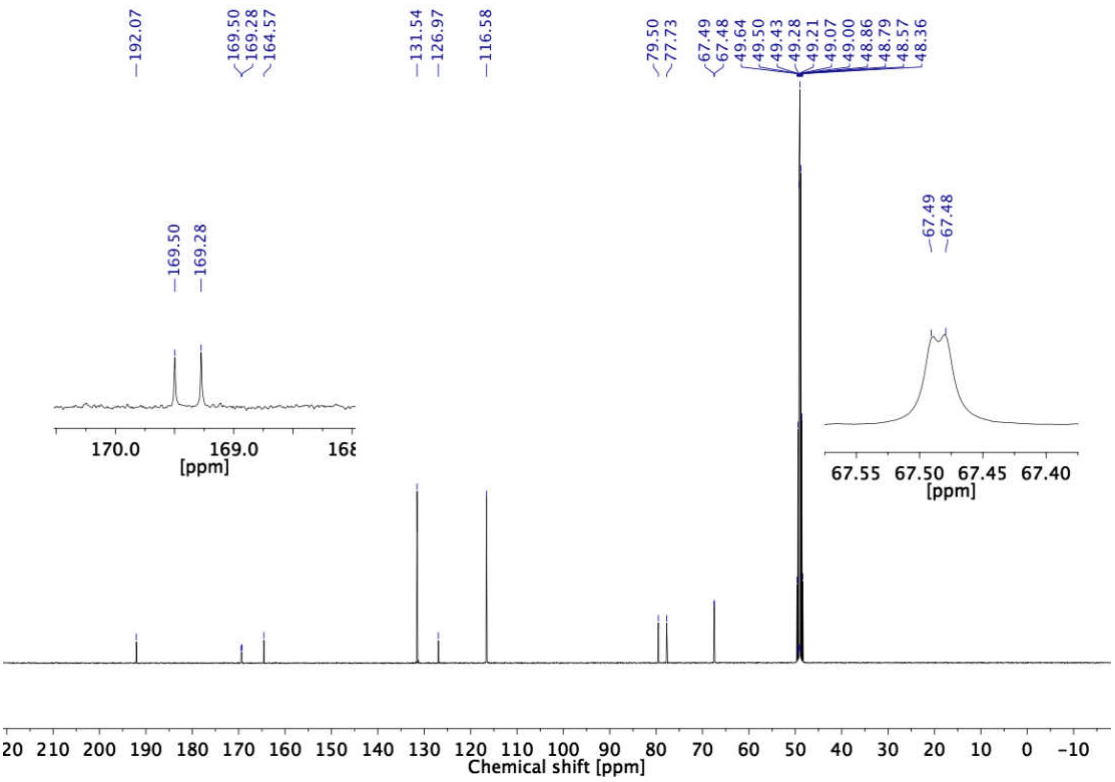

Figure SN2: ^{13}C NMR (101 MHz, 298 K, CD_3OD).

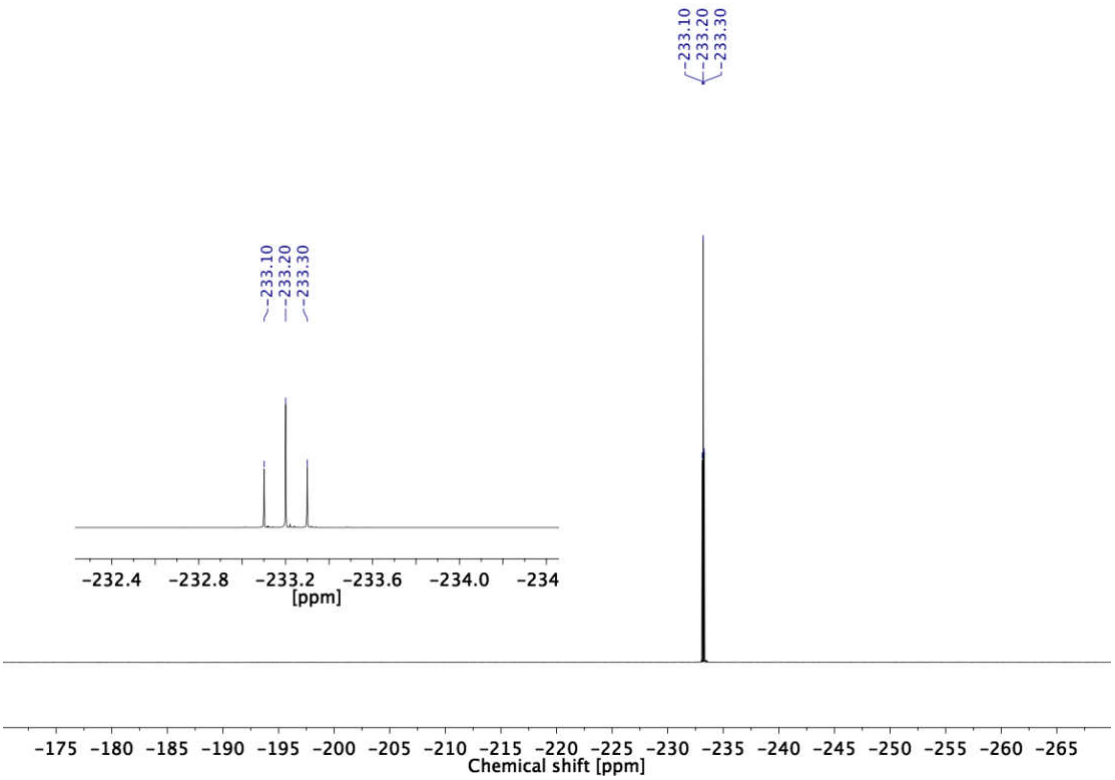

Figure SN3: ^{19}F NMR (470 MHz, 298 K, CD_3OD).